**Citation**
Shi, T. and Zhang, X. and Hao, H. and Xie, G. 2021. Experimental and numerical studies of the shear resistance capacities of interlocking blocks. Journal of Building Engineering. 44: ARTN 103230. http://doi.org/10.1016/j.jobe.2021.103230

# Experimental and Numerical Studies of the Shear Resistance Capacities of Interlocking Blocks

Tingwei Shi, Xihong Zhang*, Hong Hao, Guanyu Xie

Centre for Infrastructural Monitoring and Protection, School of Civil and Mechanical Engineering, Curtin University

*xihong.zhang@curtin.edu.au

## Abstract

Interlocking bricks could improve construction efficiency, reduce labour cost, and provide better mechanical performance for masonry structures. Nevertheless, the shear properties of mortar-less interlocking bricks have not been systematically investigated which may impede their wide applications. In this study, the shear performance of a new type of interlocking brick is investigated in detail. Laboratory shear test is firstly conducted to study the damage and shear capacity of mortar-less (dry-stacked) interlocking bricks. Numerical model is then generated with consideration of contact imperfection and validated with test results. Intensive parametric studies are conducted to quantify the influences of material strength, axial pre-compression force, friction coefficients, and contact imperfection at brick interfaces on the shear response of interlocking prisms. The accuracy of existing methods for predicting the shear capacities of shear key by design standard and empirical formula are evaluated. Based on the numerical and laboratory results, an empirical design formula is proposed to predict the shear capacity of the interlocking brick.

**Keywords:** Interlocking blocks; shear key; shear strength; numerical modelling.

## 1 Introduction

Brick structure is one of the most popular building types all over the world especially for low-rise buildings. Conventional masonry structure is constructed with mortar and bricks. Usually, the strength of mortar is lower than the brick material. Hence, damage tends to occur in the mortar layers when the structure is subjected to in-plane or out-of-plane shear force, especially when the axial loading level is relatively low [1]. Considering this deficiency, interlocking bricks with shear keys have been introduced to substitute conventional bricks to improve its mechanical performance. Besides enhanced shear resistance, interlocking bricks also have other attractive features such as improved construction efficiency with easy alignment [2, 3].

Different interlocking keys have been developed and introduced in recent years, which can provide loading resistance in vertical, horizontal or both directions. The effect of interlocking connection on brick compressive load bearing capacity has been investigated primarily through experimental methods [4-10]. Some researchers reported low compressive load-bearing capacity of interlocking bricks due to the relatively small contact area because of joint imperfection [11, 12]. Apart from compressive capacity, the shear mechanisms of brick with different interconnections have also been studied and reported [13-21], which nevertheless are mostly for validation of particular products. It shall also be worth noting that most current structures comprised of interlocking bricks are characterized by small shear keys for easiness in construction, i.e., easy alignment. The shear tenons do not remarkably improve the shear resistance of these bricks since the projection area of the keys is relatively small [22]. Recently some laboratory tests were conducted on interlocking bricks with large shear keys. Total shear off failure was found on these interlocking bricks under large axial force; and damages to the tips of the keys were discovered under low axial compression [23, 24]. Besides, recent studies by Zhang et al. [25, 26] also observed damages induced by stress concentration at shear keys of segmented columns comprised of concrete blocks with shear keys under impact and cyclic loading, which reduced column load bearing capacity against impact and seismic load. Apart from the above studies on the performances of particular designs by different researchers, the mechanical properties of interlocking brick still need comprehensive studies.

Various types and shapes of interlocking joints have been developed to improve the capacity of the interlocking bricks [27-29]. Ahmed and Aziz summarized that mortar-less joints with multiple keys had better mechanical behaviour than single key without epoxy, because multiple keys enable stress transfer uniformly between adjacent bricks and thus lead to better mechanical performance [30]. Although increasing the number of interlocking keys improves the shear capacity of joints, the equivalent shear capacity of mortar-less joints with multiple keys is less than that of mortar-less joints with single key. For example, Alcalde et al. [31] analysed the fracture behaviour of mortar-less keyed joints subjected to shear load and found that the averaged shear strength decreased with the increase in the number of keys, because the keys failed sequentially. Nevertheless, this effect became less apparent as axial prestress increased to 3.0 MPa because a higher normal compressive stress increased the friction resistance and improved the integrity of the key group. Similar results were observed by Zhou et al. [32] and Jiang et al. [33]. Moreover, changing the key geometry may also greatly influence the shear performance of keyed joints [34]. Zhang et al. [35] examined the direct shear resistances of four different shaped shear keys and concluded that they have very different shear resistance capacity and shear stiffness because of the difference in shear flow mechanism of different shaped shear keys.

The axial pre-compression level at the interlocking joint is another factor that influences the shear performance of keyed joint [27, 32, 36-39]. Higher shear strength and initial stiffness were found on interlocking joints when the axial pre-compression increases. This is because the increased axial compression could increase both the contact surface friction and the shear resistance of the interlocking key [40]. Moreover, with a higher axial pre-compression level, the post-peak ductility of the interlocking joint was also found to be improved [28]. As expected, material strength also considerably affects the initial stiffness, the ultimate shear capacity, failure modes and ductility of interlocking joint [30, 37, 38, 41]. Nevertheless, the increase in the initial stiffness of the keyed joint is not proportional to the increase of material strength. When a high strength concrete of over 80 MPa was used for the interlocking joint, limited improvement was found on the elastic stiffness of the interlocking joint [28].

For dry interlocking joints, surface roughness condition could strongly influence the shear performance of keyed joints [6, 12, 42, 43]. Martínez et al. [8] found that the uneven surface despite small could change stress distribution at the interface, and therefore affect contact pressure. Fan et al. [44] studied the contact behaviour of rock and observed both shear failure and friction failure modes which are influenced by surface roughness condition. These previous studies indicated that for mortar-less masonry construction, the surface roughness condition at the joint could significantly influence the mechanical performance, which are proved by some recent studies on mortar-less masonry prisms [45-47]. However, the influence of the surface roughness on the shear capacity has not been properly studied. It is critical for engineering application to appropriately investigate the effect of contact surface on the failure modes, as well as stress concentration in the dry-stacking masonry constructions. To investigate the effect of contact surface roughness, different methods have been applied to model rough contact surfaces. For example, Bahaaddini [48] employed discrete element method to reproduce the shear behaviour of saw-tooth triangular joints. Homogenization of the random rough surface into regular rough surface has also been a popular approach for modelling rough steel surface [49, 50]. The study of influences and modelling approaches of rough concrete and brick surface is very limited.

Different formulae for predicting the ultimate shear capacity of interlocking joints have been proposed where the difference could be substantial [30]. Some of these formulae come from theoretical derivation [51, 52], while others are empirical from laboratory testing and numerical modelling [36, 53, 54]. Most popularly used design code such as AASHTO [55] assumes the shear force is transferred through the interlocking joint by both the shear key and surface friction [28]. Some researchers evaluated the accuracy of AASHTO method in predicting the shear resistance capacity of different keyed joints. For example, Ahmed and Aziz [56] carried out direct shear test to study the shear behaviour of mortar-less connections with single and multiple keys. It was found that the AASHTO design formula could conservatively predict the shear strength of joints with single key, but overestimate the shear strength of mortar-less with multiple keys. Similar results were also reported by Zhou et al. [32]. However, opposite conclusion was reported by Jiang et al. [33] who found AASHTO method underestimates the shear load of joints with single key made of steel fibre reinforced concrete (SFRC) but more accurately predicts that of three-keyed dry joints. For interlocking brick comprising multiple keys, the accuracy of AASHTO and other prediction methods are not known yet.

In this paper, laboratory tests and numerical simulations are performed to investigate the shear behaviour of interlocking brick prisms. Laboratory shear tests are firstly conducted on interlocking brick prisms under different axial pre-compressions. Then, a detailed numerical model considering contact surface roughness is generated and validated with testing results. Parametric studies are then carried out to investigate the influence of different design parameters. An empirical formula is proposed to predict the shear capacity of the mortar-less interlocking brick prism, which can be used in engineering practice to quickly estimate the shear capacities of interlocking brick structures with varying material properties, loading conditions, and brick surface conditions.

# 2 Laboratory Tests

Laboratory shear test is carried out to experimentally examine the shear behaviour of interlocking bricks. Considering the large variation in brick material properties, the material strength of the studied interlocking bricks is firstly tested through unconfined uniaxial compressive test. Then, shear test on interlocking brick prisms is setup and performed to investigate the shear behaviour of interlocking bricks.

## 2.1 Material property

The interlocking bricks used in the laboratory test are made of cement stabilised rammed earth material. To determine the brick material properties, uniaxial unconfined compressive tests are conducted using a SHIMADZU-50 machine in Structural Laboratory of Curtin University. Brick cores with a height of 100 mm and a diameter of 50 mm are drilled out of interlocking bricks, and carefully grinded on both the top and bottom, as shown in Figure 1a. Strain gauges are sticked onto the specimen surfaces to acquire the axial strain. Following ASTM C140 [57], in the test a loading speed of 0.03 mm per second is adopted to apply the axial compressive load using displacement control method. The averaged axial stress-strain curve measured in the laboratory tests are shown in Figure 1b, where the axial stress is calculated by dividing the measured axial compressive load by the cross-sectional area of the specimen. Strain gauges are used to measure the axial strain. The numerical prediction of the corresponding stress-strain curve is also presented in the figure, details of numerical model will be presented in the subsequent sections.

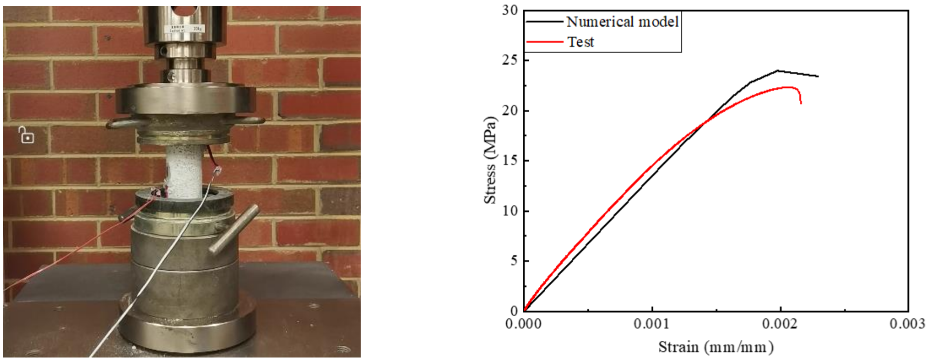


(a) Uniaxial compressive test (b) Stress–strain curves

*Figure 1. Determination of brick material properties*

## 2.2 Shear test setup

Following BS EN 1052-3 [58], shear tests are setup to examine the shear properties of the interlocking bricks. Figure 2a and b illustrates the test setup, where the specimen dimension is 600mm × 200mm × 200mm (length × height × thickness). The prism comprises of three dry-stacking interlocking blocks of 200mm ×100mm ×180mm (length ×thickness×height) and two pieces of half bricks as end blocks. The interlocking blocks have large interlocking keys (35 mm length × 35 mm thickness× 30 mm height), which provide shear resistance at the interlocking joints, as shown in Figure 2c. The prism is firstly pre-loaded axially in the horizontal direction. Then, the two side blocks are fixed using two steel plates to the bottom supporting frames. To minimize the flexural bending deformation in the prism, flat bars and wide-angle plates are used to fix the two end bricks firmly to the bottom support frame. The rotation of the two side bricks is therefore effectively restrained. Displacement controlled loading method is applied where the central block is pressed to move downwards at a speed of 1.8 mm per minute. Two shear planes are therefore created through this setup. Because of the non-symmetric layout of the interlocking keys on the brick, the damage and failure of the testing brick prism vary on the frontal surface (Side I) and rear surface (Side II).

One LVDT (linear variable differential transformer) is installed to record the vertical displacement of the central brick. Another LVDT is used to measure the vertical movement of one side brick, so as to monitor the rotational movement of the side brick. One loadcell is used to monitor the axial pre-compressive force applied. Another loadcell is used on the central brick to measure the shear force applied to the shear planes. Two loadcells are installed beneath the two side bricks to ensure the same amount of tying forces is applied. Two groups of tests are conducted with 10 kN and 30 kN axial pre-compression applied to the brick prisms, corresponding to 0.538 MPa and 1.614 MPa axial stress, which are the typical vertical stress in masonry wall for a single-storey and low-rise masonry building. Three specimens are tested for each group in the study.

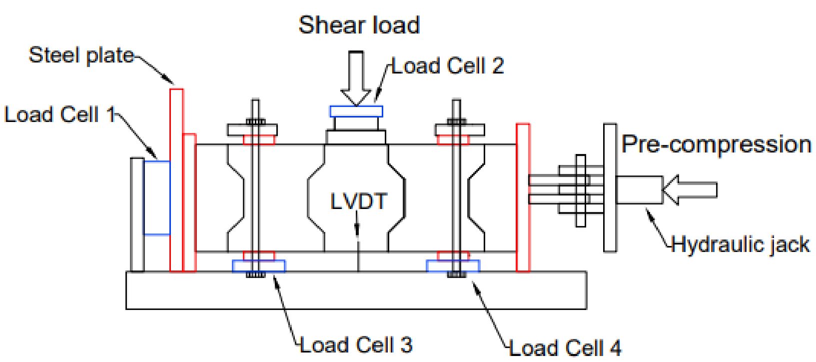

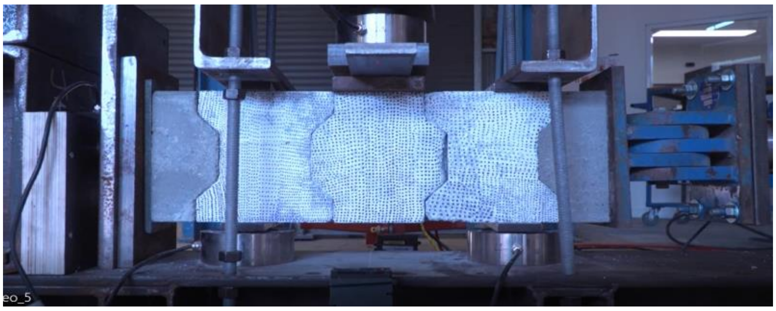

(a) Illustration of test setup

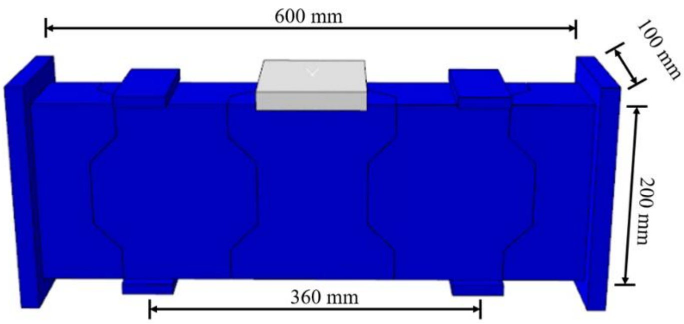


(b) Numerical model

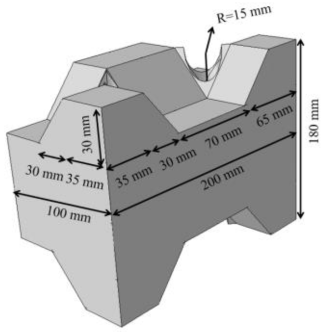


(c) Configuration of interlocking blocks

Figure 2. Experimental and numerical models for the prism shear test

## 3 Numerical Simulation

A three-dimensional finite element model of the interlocking brick prism is developed in Abaqus [59] to further investigate the shear behaviour of the interlocking bricks.

### 3.1 Model details

Figure 2b presents the numerical simulation of the interlocking prism, which replicates the laboratory test setup. Steel strips of the same dimensions as in the test are modelled to fix and load the brick prism, where a friction coefficient of 0.15 is adopted between steel and the bricks [8]. Solid element C3D8R in Abaqus is adopted for the interlocking brick. In the numerical modelling, three loading steps are implemented, i.e., axial pre-compression of the interlocking prism, fixing the two side bricks with vertical pre-tying force onto the two supports, and application of vertical load on the central brick. The axial pre-compressive force and pre-tying force are applied using force control method. For the vertical force, displacement-controlled loading method is used as in the laboratory test. Convergence study is implemented by step-reducing the mesh sizes. It is found that when the mesh size reduces from 5 mm to 2.5 mm, the maximum compressive force in the prism does not change much but it requires a significantly higher computation resource. Therefore, 5 mm mesh size is used in this study for the numerical simulation.

## 3.2 Material model

The material model of concrete damage plasticity (CDP) is employed to simulate the nonlinear behaviour and damage of the brick, which is proposed by Lubliner et al. [60]. Crushing in compression and cracking in tension can both be modelled. As shown in Figure 3, in CDP model, the compressive and tensile stress-strain relationships are defined, which are featured by damaged plasticity parameters. The unconfined uniaxial compressive strength is acquired via the laboratory material tests depicted in Section 2.1. The elastic modulus ($E_0$) is taken as the secant modulus determined from the origin to the point with a stress level equivalent to 40% of the compressive strength. The Poisson's ratio is determined at the same stress level. Table 1 and Table 2 show the material properties of the interlocking brick, where $E_0$ represents the elastic modulus; $v$ denotes the Poisson's ratio. The tensile strength is taken as $f_t$=0.1 $f_c$ following previous studies [8, 61]. The unconfined uniaxial compressive behaviour of the brick core is modelled to verify the brick material constitutive model. The stress-strain curve from the numerical calculation using the CDP model agrees reasonably well with that in the laboratory test (see Figure 1b). The compressive and tensile damage parameters ($d_c$ and $d_t$ in Figure 3) can be calculated following literature [62]. An elastic perfect plastic material model is adopted for the steel, whose Young's modulus of 210 GPa as well as Poisson's ratio of 0.3 are used.

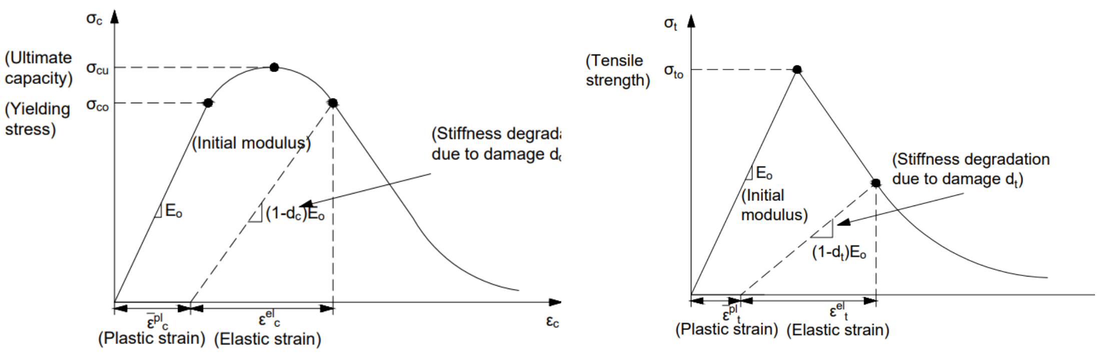


(a) Compression (b) Tension

*Figure 3. Definitions of concrete damage plasticity (CDP) model* [53]

*Table 1. Material properties of interlocking brick*

| Elasticity | | Plasticity | | | |
|---|---|---|---|---|---|
| Initial Young's modulus, | Poisson's ratio $\upsilon$ | Dilatation angle $\psi$ (°) | Eccentricity | Biaxial stress | K |

| $E_0$ (GPa) | | | | ratio $f_{bo}/f_{co}$ | |
|---|---|---|---|---|---|
| 13.49 | 0.2 | 30 | 0.1 | 1.16 | 0.67 |

*Table 2. Material constants of concrete damage plasticity model*

| Behaviour in compression | | Behaviour in Tension | |
|---|---|---|---|
| Yield stress (MPa) | Inelastic strain | Yield stress (MPa) | Cracking strain |
| 15.12 | 0 | 1.78 | 0 |
| 15.96 | 0.00002 | 0.93 | 0.0007 |
| 16.84 | 0.00006 | 0.78 | 0.0008 |
| 17.84 | 0.00012 | 0.63 | 0.0009 |
| 10 | 0.0010 | 0.48 | 0.0010 |
| | | 0.18 | 0.0012 |

## 3.3 Contact algorithm

Contact surface strongly influences the behaviour of mortar-less joint of interlocking bricks [6]. Three different modelling approaches: perfect contact, random rough contact and simplified rough contact, are used to simulate the contact behaviour between the mortar-less joints.

### 3.3.1 Perfect contact

The perfect contact is the simplest approach used in the engineering field. It assumes that contact surfaces between neighbouring bricks are smooth, which leads to perfect connection. The surface-to-surface contact is used to simulate the connections between the neighbouring interlocking bricks. The tangential behaviour is defined by Mohr-Coulomb criterion, the friction coefficient is taken as 0.3 [8, 63]. And the normal behaviour is defined by hard contact. The hard contact ensures contact surfaces between the adjacent interlocking bricks be in contact without penetration.

### 3.3.2 Random and simplified rough contact

The random rough contact considers brick natural surface condition due to material and manufacture tolerance. To examine the true brick surface condition, laboratory test is carried out using a laser profile scanner to quantify the surface profile of the bricks. As shown in Figure 4a, each brick is cut into halves and placed on a flat testing table, and the laser scanner installed on a rigid steel frame scans the top surface profile of the interlocking brick. The laser scans the surface for three times, and the averaged value of profile is taken as the actual surface roughness. Figure 4b shows one of the typical brick surface contours scanned from the test. The above experimentally measured contour at the interlocking bricks is then numerically generated with fine mesh as illustrated in Figure 4c. To improve computational efficiency, and also to reasonably model surface roughness without the need to measure every surface of the interlocking bricks, the random surface roughness is simplified by the mean surface roughness value and trapezoidal shape roughness profiles (Figure 4c).

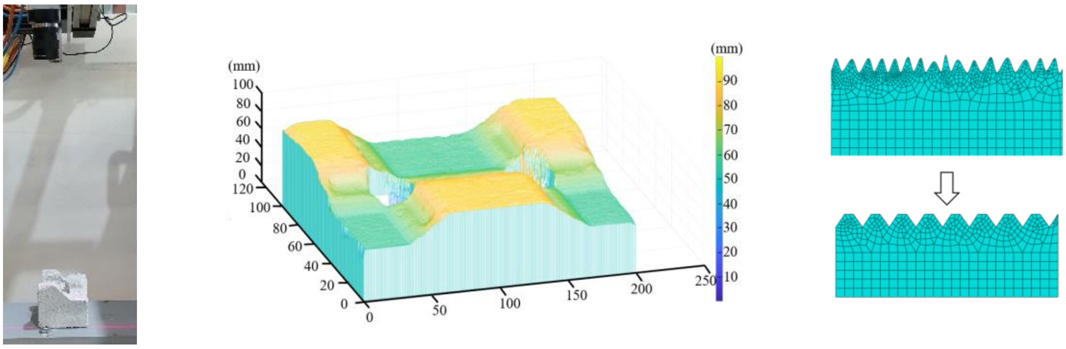


(a) Laser scanning brick surface roughness | (b) Measured contour of a typical surface roughness | (c) The equivalent rough surface

*Figure 4. Evaluation of brick surface roughness*

## 4 Results and Analysis

Numerical modelling and laboratory testing results are provided in this section. Shear load-displacement relationship, failure modes of the interlocking brick, and shear capacity are compared to demonstrate the shear behaviour of interlocking bricks.

### 4.1 Load-displacement curves

Figure 5 presents the shear load versus central brick vertical displacement. In this paper, a half of the applied vertical force is taken as the "shear force" experienced by the interlocking joint due to the two symmetric shear planes, and this shear force is taken as the shear capacity of the interlocking joint. Without losing generality, Specimen 2 is taken as an example, when a 10 kN axial pre-compression is applied to the brick prism, the shear force increases linearly to about 6.27 kN at about 0.11 mm displacement, reflecting an initial stiffness of 56.43 kN/mm, and it corresponds to about 30% of the maximum shear load of the prism. As the shear load further increases, the slope of the curve drops. The shear load increases non-linearly as it approaches the maximum shear load of 21.18 kN at a displacement of around 1.46 mm, after which it begins to decrease, reflecting the failure of the interlocking prism. Similar trend can be found on Specimen 1. It is worth noticing that on Specimen 3 after the initial peak load is reached, a 2$^{nd}$ peak load is developed. The first peak corresponds to the damage of intact prism at the weakest shear key and the sharp drop reveals shearing off on one side of the shear key that provides the shear strength $\tau_1$. Afterwards, stress at the interlocking connection is redistributed, where block rotation can be observed. The test might be influenced by the flexural bending deformation of the prism, which was observed in the lab test. The second peak represents the combined contributions from the shear strength of the second interlocking key, some friction force in the first interlocking key connection due to bending, and membrane effect due to the prism deformation and axial pre-compression. Therefore, a higher shear force is recorded for the 2nd peak load. Similar observation was reported by previous researchers on the concrete shear key [64]. Nevertheless, it is worth noting that because of the large depth, the prism can be considered as a deep beam, whose flexural deformation is therefore not significant. Some variations among the three prisms tested can be observed, which are due to the inherent variability of contact surfaces between mortar-less interlocking bricks and the non-simultaneous damages of the interlocking bricks at the two shear planes.

When the prisms are subjected to 30 kN axial pre-compression, similar behaviours can be observed, but with a larger initial stiffness. Typically for Specimen 6, the initial stiffness is 88.30 kN/mm due to the higher axial pre-compression. A peak shear load of about 29.58 kN is achieved at around 0.88 mm displacement. After reaching the maximum shear force, the applied force decreases steadily with further increased displacement until residual strength is maintained. Larger peak shear resistance is observed on the 30 kN pre-compressed prisms as compared to that of the 10 kN pre-compressed prisms because the increased axial compression leads to higher inter-surface friction [29].

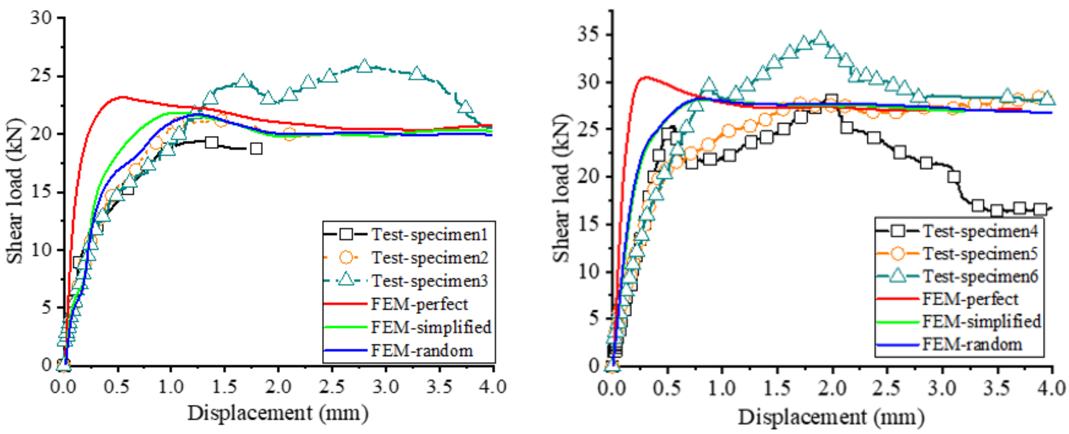


(a) 10 kN axial pre-compression (b) 30 kN axial pre-compression

*Figure 5. Load-displacement curves from numerical simulation and laboratory test*

The numerically modelled shear force-displacement curves are compared with those from the laboratory tests, as shown in Figure 5. It can be observed that the perfect contact models largely overestimate the initial stiffness of the interlocking prisms under both 10 kN and 30 kN axial pre-compression cases. In comparison, the numerical models with random and simplified rough surfaces could more closely replicate the stiffness of the prism. For example, under 10 kN axial pre-compression, the perfect contact model predicts an initial stiffness of 136.87 kN/mm, while the simplified and random rough contact models predict 50.86 kN/mm and 38.88 kN/mm, respectively. Similarly, under 30 kN axial pre-compression, an initial stiffness of 188.31 kN/mm is predicted by the perfect contact model, which is much higher than those of 102.96 kN/mm and 107.75 kN/mm by the random and simplified contact model. Nevertheless, these three models predict similar shear loading capacities. For example, under 10 kN axial pre-compression, the perfect contact model predicts a maximum shear load of 23.17 kN in comparison to 21.86 kN and 21.69 kN for the simplified and random rough contact models indicating less than 10% difference. Similar trend can be found for the interlocking bricks under 30 kN axial pre-compression. It is evidenced that modelling of contact surface is crucial for accurate predictions of interlocking brick shear stiffness and capacity, under higher axial pre-compression, the difference between the random and simplified rough surface models is smaller. The simplified and detailed random rough surface models predict very similar shear capacity because the shear resistance is primarily provided by the shear key, while the contribution of the surface friction that is closely related to surface roughness condition is not pronounced. These results indicate that the random rough surface can be approximately modelled by simplified trapezoidal rough surface, which give similar predictions of the shear capacity, and close predictions of the shear stiffness especially when the axial compression force is relatively large.

## 4.2 Failure mode and crack propagation

In the numerical simulation, crack initiation and evolution can be depicted by the damage contour since continuum element with damage based material model is employed [65]. Because of the unique shape of the interlocking bricks, there are two different failure patterns on the frontal and rear sides of the interlocking brick prism as shown in Figure 6, i.e., Side I and II. On Side I diagonal cracks are developed on the bottom shear keys of the two side bricks. This is accompanied by a brittle shear failure at the shear keys because of the principle stress on the plane reaching the failure strength [52]. Similarly, on Side II cracks initiate on the corner of the tenon of the central brick, and then the cracks extend shortly in the direction perpendicular to the inclined surface after which the cracks propagate vertically. Thus, the crack pattern on Side II is a mixed crack mode (Figure 6b). The excessive shear stress leads to the eventual damages of these tenons. After the failure of these tenons, only surface friction at the interfaces resists the shear load which provides the residual shear capacity.

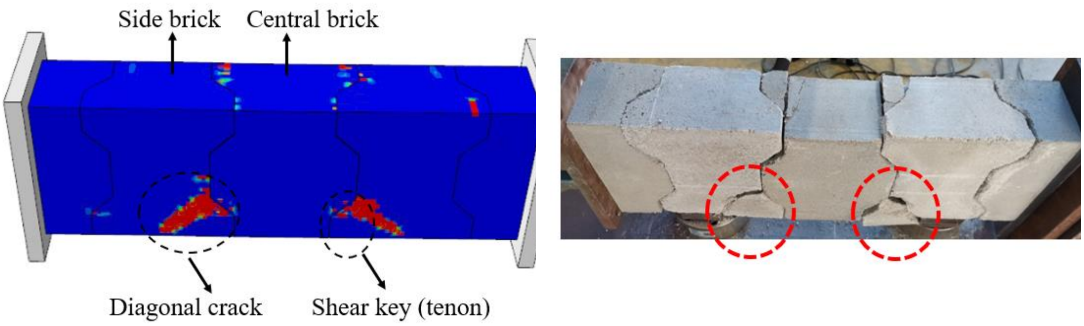

(a) Side I

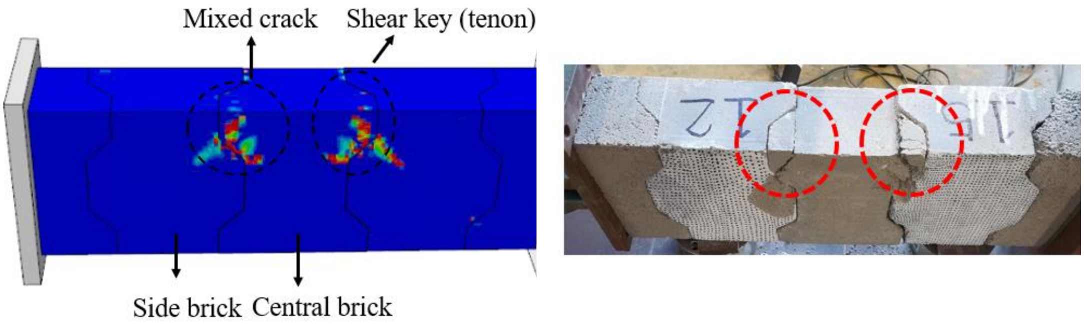

(b) Side II

*Figure 6. Comparison of prism damage modes between numerical modelling and laboratory test*

The crack initiation and propagation processes of the interlocking brick prism modelled numerically and recorded in the lab test are plotted in the shear force versus displacement curve as shown in Figure 7. As can be observed on Side I diagonal cracks initiate on the bottom shear keys of the two side bricks at Stage A. They extend diagonally at about 45°, associated with the slight decrease in the stiffness of the specimen. With further applied vertical displacement on the central block, cracks further develop leading to the further damage of the interlocking brick prism. Unlike the numerically modelled cracks occurred simultaneously and symmetrically on both sides of the interlocking brick prism, crack in the laboratory tested specimen occurred only on one side first because of unavoidable asymmetry of the tested specimens owing to imperfectness in preparing the bricks and interlocking specimens. But at the maximum shear load, the crack patterns converge between numerical modelling and experimental observation. It can also be observed from Figure 7 that on Side II the shear key of the central brick cracks under the applied shear load at Stage A, which extend diagonally at about 45° angle. With the further increased shear load, the cracks then extend vertically and penetrate through the central brick at the maximum shear load.

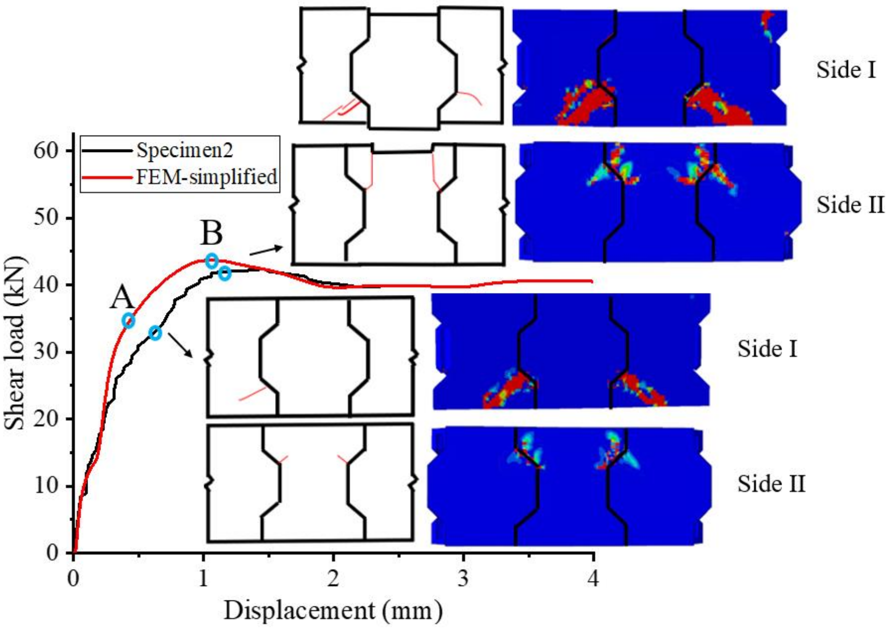


*Figure 7. Prism cracks evolution in the numerical simulations and experiments (Specimen 2 under 10 kN axial pre-compression)*

## 4.3 Stress distribution and crack evolution

To better understand the stress distribution in the interlocking brick prism, the tensile stress and shear stress contours generated from the numerical modelling using the simplified rough surface model are plotted along with the shear load versus displacement curves in Figure 8. On Side I, the applied shear force on the shear plane induces a large tensile stress around the shear key of the side brick. At Stage A, diagonal crack appears due to excessive tensile stress at the shear key, which extends and propagates under the further increased shear force on the interlocking joint. For the central block on Side II (Figure 8b), a large tensile stress is generated around the shear key because of geometry change induced stress concentration. Tensile cracks (mode I) are initiated at Stage A, which extend diagonally at about 45°. As the applied shear load gradually increases, the propagation of diagonal cracks ceased because it enters a low tensile stress field which therefore would release less strain energy. The formation and propagation of the diagonal crack results in the rotation of the shear key and varies the boundary condition of the stress zone. As a result, a large shear stress is induced around the shear key (as in Figure 8b), which consequentially leads to the further development of the crack under the shear stress (mode II crack) until the total failure of the shear key on the central block at Stage B.

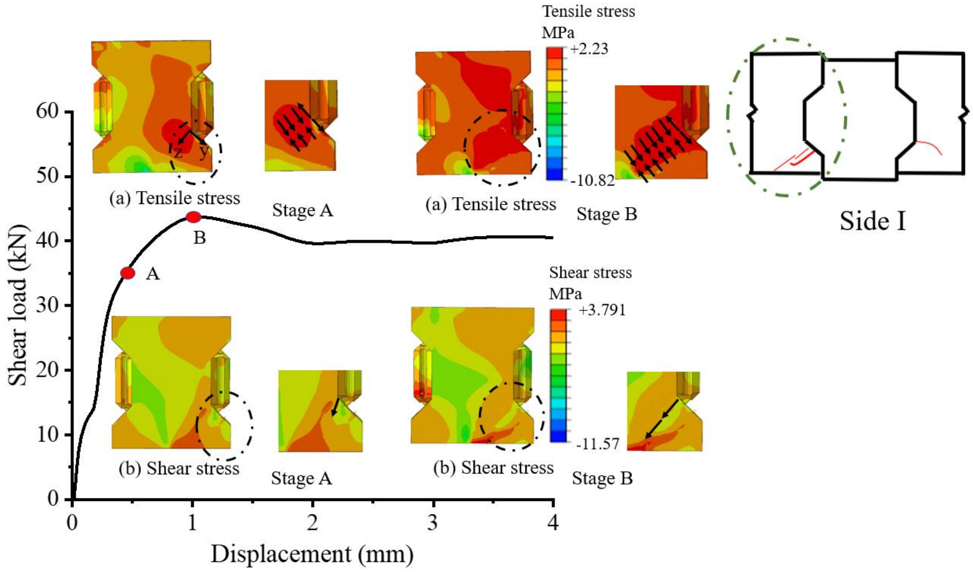


(a) The diagonal crack evolution in the side brick on Side I

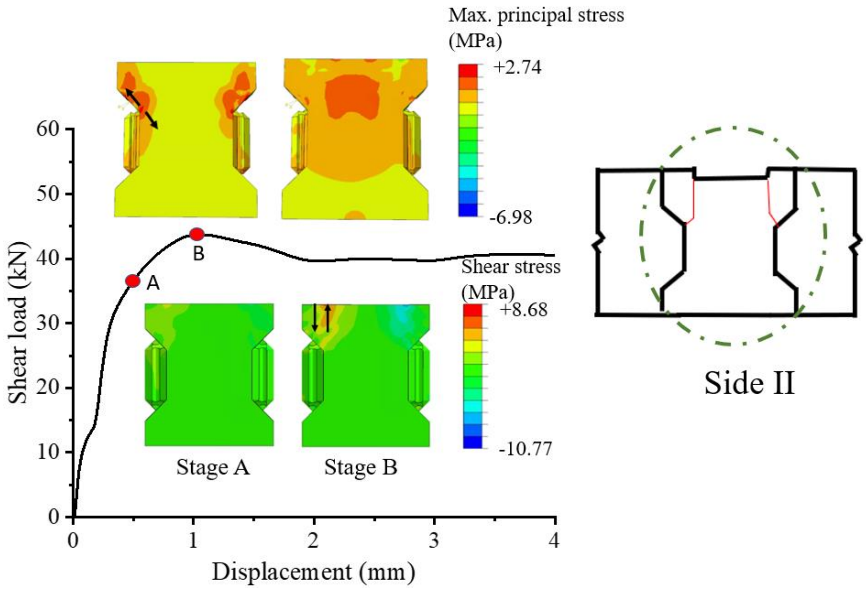


(b) The mixed crack evolution in the central brick on Side II

*Figure 8. Crack evolution of prism stress contours*

## 4.4 Shear capacity

To examine the shear capacity of the interlocking prism, the wedge crack model (WCM) [66] is employed. As illustrated in Figure 9, the vertical force from the shear load on the interlocking joint is $F$ and the horizontal force from axial compression acting on the cracking area is $F'$, which leads to the crack initiation. The stress intensity factor of mode I crack [67] at the crack tip, generated by the wedging forces $F$ and $F'$ ($K_{Ia}$), can be given as follows:

$$K_I = 2(Fsin\theta - \mathrm{F}'cos\theta)\sqrt{\frac{\pi}{(\pi^2-4)l}} \tag{1}$$

where $l$ stands for the length of the diagonal crack; subscription I represents mode I crack. The crack angle $\theta$ is assumed to be 45° following laboratory observation and previous studies [68-70]. For mode I fracture, crack is initiated when the stress intensity factor $K_I$ reaches $K_{IC}$, where $K_{IC}$ =0.0443 MPa·m$^{1/2}$ denotes the fracture toughness of material [71]. Therefore, the maximum shear capacity $V$ for the interlocking brick at the joint can be expressed as:

$$\begin{aligned} V = F_{pre}\mu &+ \left(K_{IC}\sqrt{\frac{(\pi^2-4)l_1}{\pi}}\times\frac{1}{2} + F_1'cos\theta\right)\frac{1}{sin\theta} \\ &+ \left(K_{IC}\sqrt{\frac{(\pi^2-4)l_2}{\pi}}\times\frac{1}{2} + F_2'cos\theta\right)\frac{1}{sin\theta} \end{aligned} \tag{2}$$

Where $F_{pre}$ is the axial pre-compressive force on the interlocking prism, and $\mu$ is the surface friction coefficient, which equals to 0.3. The term $F_{pre}\,\mu$ in Eq. (2) accounts for the friction resistance force at the interlocking joint. Substituting crack lengths $l_1$=10mm for the central brick and $l_2$=88mm for the side bricks, the maximum shear capacity $V$ for the interlocking brick can be calculated.

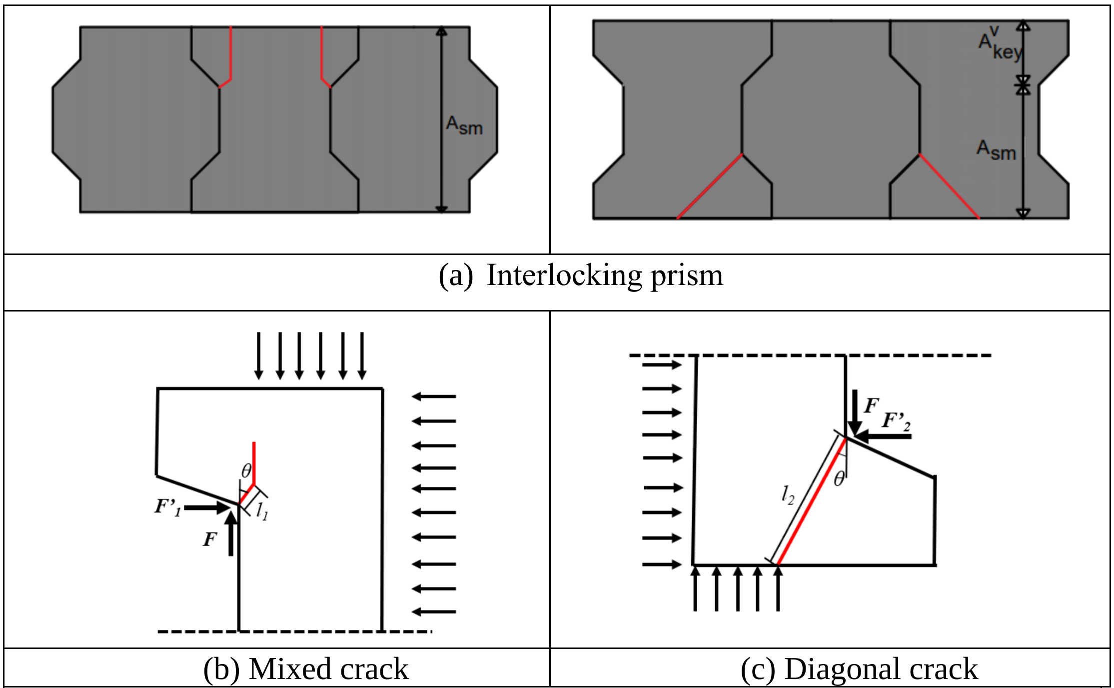


(a) Interlocking prism

(b) Mixed crack

(c) Diagonal crack

*Figure 9. Load analysis for the wedging action on interlocking bricks*

In the meanwhile, following design code EN-1052-3 [58], the equivalent shear strength for the interlocking bricks can be calculated for simplified engineering application by assuming two shear planes created between the central block and the two side blocks as shown in Figure 6. The equivalent shear strength is calculated using the shear load on the interlocking joint (one shear plane) dividing the cross-sectional area of the joint (200mm height × 100mm depth minus the area of two holes). Table 3 summarizes the peak shear load on the interlocking joint ($V_1$), the equivalent shear strength ($\tau_1$), the associated displacement ($\delta_1$) and the initial shear stiffness. Among the three specimens of each group of tests, a coefficient of variation (CoV) about 10% is found which indicates that the test results vary in an acceptable small range. When subjected to 10 kN axial compression, an averaged equivalent shear strength of 1.17 MPa is measured, which is 27% lower than that under 30 kN axial pre-compression (1.48 MPa). This is expected as axial pre-compression could influence both the friction resistance and the shear resistance of the shear key. Therefore, axial pre-compression level should be considered when evaluating the shear strength of interlocking bricks.

*Table 3. The results obtained from the shear tests*

| Prisms | $V_1$/kN | $\tau_1$/MPa | $\delta_1$/mm | Initial shear stiffness/(kN/mm) |
|---|---|---|---|---|
| Preload-10-1 | 19.42 | 1.04 | 1.31 | 57.12 |
| Preload-10-2 | 21.18 | 1.14 | 1.46 | 56.42 |
| Preload-10-3 | 24.51 | 1.32 | 1.74 | 53.00 |
| Average | 21.70 | 1.17 | 1.50 | 55.51 |
| Preload-30-1 | 25.31 | 1.36 | 0.54 | 107.40 |
| Preload-30-2 | 27.80 | 1.50 | 1.75 | 164.00 |
| Preload-30-3 | 29.58 | 1.59 | 0.88 | 163.51 |
| Average | 27.56 | 1.48 | 1.06 | 144.97 |

## 4.5 Comparison with design formula

Comparison is made between the above tested shear capacity for the interlocking brick and existing empirical formula and design method to evaluate the accuracy and suitability of these existing methods. In engineering practice, AASHTO design code (in Eq. (3)) [55] and the semi-empirical formula proposed by Rombach and Specker [32, 72, 73] (in Eq. (4)) are the commonly used methods. As shown, both methods separate the shear capacity $V$ of a keyed joint into two parts: a) resistance from the interlocking key; and b) interface friction.

$$V = A_{key}^{V}(0.006792 f_{cm})^{0.5} \times (12 + 2.466\sigma_n) + \mu A_{sm}\sigma_n \tag{3}$$

$$V = 0.14 f_{cm} A_{key}^{V} + 0.65(A_{key}^{V} + A_{sm})\sigma_n \tag{4}$$

where $A_{key}^{V}$ is the projection area of shear keys on the failure plane (mm$^2$); and $A_{sm}$ is the contacting area between flat contact surfaces in the failure plane (mm$^2$), as shown in Figure 9a; $f_{cm}$ is the characteristic compressive strength of material (MPa); $\sigma_n$ is the average compressive stress across the key base area (MPa); and $\mu$ is the friction coefficient between the contacting surfaces, which AASHTO recommends as 0.6.

*Table 4. Comparison of shear capacities between laboratory testing results, numerical modeling and existing empirical and design formulae*

| Pre-load kN | Maximum shear force kN | Numerical simulation kN | error % | AASHTO kN | error % | Rombach & Specker kN | Error % | Theoretical prediction kN | error % |
|---|---|---|---|---|---|---|---|---|---|
| 10 | 21.70 | 21.86 | 0.74 | 21.19 | -2.37 | 15.29 | -29.55 | 22.04 | 1.57 |
| 30 | 27.56 | 28.16 | 2.18 | 34.16 | 23.96 | 28.29 | 2.64 | 32.09 | 16.44 |

Note: AASHTO, Rombach & Specker and Theoretical prediction denote the results from Eq. (3); Eq. (4); and Eq. (2), respectively.

Table 4 compares the shear capacity of the interlocking bricks under different axial pre-compressions and those estimated by AASHTO, Rombach and Specker's formula and the theoretical derivation presented above. Rombach and Specker carried out parametric study using numerical modelling and provided an empirical formula for estimation of the shear capacity of interlocking joint [73, 74]. Comparing the prediction results using their formula with the current testing results, it can be found that Rombach and Specker's formula substantially underestimates the shear capacity by about 30% when the prism is subjected to 10 kN axial pre-compression. This is because in their study, very small concrete shear keys were considered and direct key shear off failure was the primary failure mode, which differs to the failure mode of the interlocking brick prims in this study. As the axial pre-compressive force applied to the prism increases, the prediction error using Rombach and Specker's formula reduces, which only slightly overestimates the 30kN pre-compression cases by 2.64%. This is because the contribution percentage of friction resistance in the overall shear capacity increases and that of shear key reduces with the increase in axial pre-compression. As a result, the relative error reduces. The AASHTO formula predicts different shear capacities of the interlocking brick prism, which slightly underestimates the shear capacity of the interlocking prism by -2.37% when 10 kN axial pre-compression is applied, but it overestimates the prism shear capacity by 23.96% when it is subjected to 30 kN axial pre-compression. This prediction error by the AASHTO formula could be attributed to the following two reasons: firstly, the AASHTO formula is empirically derived based on a large amount of testing data on concrete joints with small shear keys, which being similar to the Rombach and Specker's method is not necessarily suitable for prediction of the shear capacity of large shear key. Secondly, AASHTO specifies a large friction coefficient of 0.6, which could overestimate the friction resistance at the joint between interlocking bricks. Therefore, under low axial pre-compression, AASHTO method underestimates the shear resistance of the shear key but overestimates the friction coefficient, whose effects cancel each other and ends up a closer match with the lab testing results. But when the axial pre-compression level is high, the contribution of friction becomes more pronounced. The AASHTO method gives a much higher prediction on the shear capacity of interlocking bricks, which is very similar to the observation given by Zhou et al. on the precast concrete joint, who reported consistently higher shear capacity was predicted using AASHTO method than that using the Rombach and Specker's formula. Therefore, the existing methods may not accurately predict the shear capacity of interlocking bricks. The theoretical derivation based on fracture mechanics theory overestimates the shear capacities of the interlocking brick prism by +1.57% and +16.44% when subjected to 10 kN and 30 kN pre-compression, respectively. This is possibly because the rough surface of the interlocking bricks is not considered, and thus the friction resistance estimation is not accurate.

# 5 Parametric study

To evaluate the influence of several design parameters on the shear capacity of interlocking bricks, and to derive an empirical formula for prediction of the shear capacity of interlocking bricks for engineering applications, parametric studies are carried out by varying the axial pre-compression level, surface friction coefficient, contact surface roughness, and concrete strength.

## 5.1 Effects of axial pre-compression and concrete strength

To quantify the influences of axial pre-compression and brick material compressive strength on the maximum shear load bearing capacity of the interlocking brick prism, a number of numerical simulations are conducted. The dimension of the brick is 200 mm × 100mm ×180 mm (length ×thickness ×height) as default. The mean brick surface roughness is assumed to be 0.3 mm, and the coefficient of friction is 0.3, which are based on the default brick configuration. Four different axial pre-compression levels are modelled, i.e. 0.538 MPa, 1.073 MPa, 1.614 MPa and 2.152

MPa, which correspond approximately to the axial stress levels in a ground floor wall for single- or low rise multiple-storey buildings [75]. Three different material strengths with $f_c$=10 MPa, 18 MPa, and 25 MPa are considered which are commonly used for concrete masonry units. Figure 10a shows the equivalent shear strength versus axial pre-compressive stress. As shown, the equivalent shear strength increases with the axial pre-compressive stress. For example, for the interlocking prism with material strength of 25 MPa, the equivalent shear strength is 1.56 MPa when it is subjected to a 0.538 MPa axial pre-compressive stress, and it increases to 2.09 MPa when axial pre-compressive stress is 2.15 MPa. The relationship between concrete strength and the equivalent shear strength is shown in Figure 10b. As expected, brick material strength also strongly influences the brick shear strength. For instance, as the material compressive strength increases from 10 MPa to 25 MPa, the equivalent shear strength of the interlocking brick prisms (under 2.152 MPa axial pre-compressive stress) increases by +62.06%.

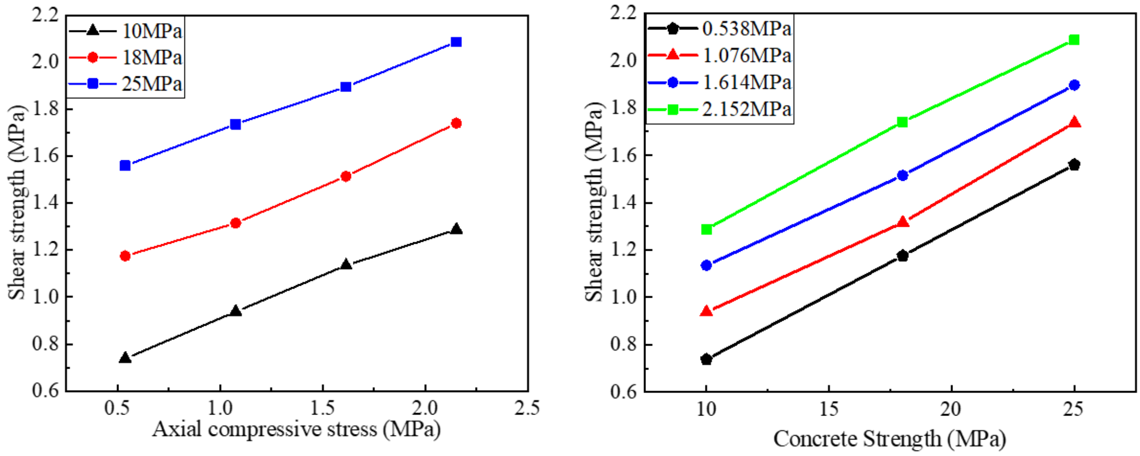


a) b)

*Figure 10. Relationships between a) prism equivalent shear strength with axial compressive stress; b) prism equivalent shear strength with concrete strength*

## 5.2 Effect of surface roughness and friction coefficient

Both the shear resistance of the interlocking shear key and the interface friction contribute to the shear resistance at interlocking joint. Interface friction as a macro-level effect and surface roughness as a micro-level effect could both influence the friction induced shear resistance of interlocking bricks. To quantify the influence of interface friction coefficient on the prism shear capacity, a sensitivity analysis is carried out, where a mean brick surface roughness is assumed to be 0.3 mm, the axial pre-compression is 30 kN, the material strength is 18 MPa, and the dimension of the interlocking brick is as default. Friction coefficient $\mu$ is varied from 0.1 to 0.6 with a 0.1 increment. Figure 11 shows the modelling results. It can be observed that with the increase of friction coefficient from 0.1 to 0.6, the initial stiffness increases from 71.74kN/mm to 126.29kN/mm by 76%. This is because a large shear force is needed to initiate the inter-block slip when the friction coefficient increases. The peak shear resistances of the interlocking brick prisms also increase as the friction coefficient increases. With friction coefficient increases from 0.1 to 0.6, the peak shear load increases from 26.12kN to 32.19kN by 23.24%. This is expected because friction resistance contributes to the shear capacity of the interlocking brick.

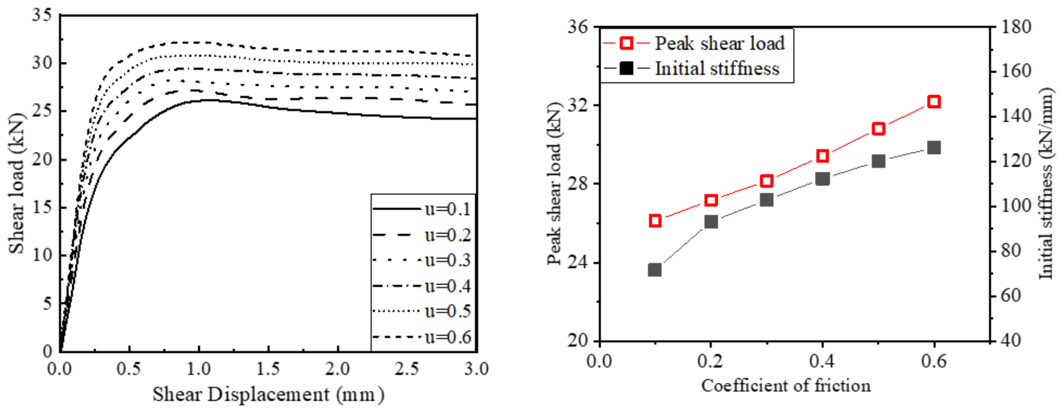


a) b)

*Figure 11. Effect of surface friction coefficient on a) shear load-displacement curves and b) peak shear load and initial stiffness*

To quantify the influence of brick surface roughness on the shear resistance of the interlocking prism, surface roughness with height ranging between 0.1 and 0.5mm at an interval of 0.1mm is numerically modelled on the interlocking bricks. The unconfined uniaxial compressive strength of the brick material is 18MPa; the axial pre-compression varies from 10 kN to 40 kN, and the friction coefficient is 0.3. The shear force versus displacement relationships of specimens with different surface roughness conditons as shown in Figure 12. For the interlocking brick prisms under 10 kN and 20 kN axial pre-compression, non-linear behaviour can be observed in the rising sections of the curves when the surface roughness is above 0.2 mm. This is because of the local compaction of the rough surfaces under axial compression, which is not obvious when the surface roughness is 0.1 mm. Under a higher axial pre-compression, this non-linear behaviour becomes unrecognizable. It can also be observed that with increased surface roughness, the displacement at the peak shear load increases. This is because a larger displacement is needed for the asperities in the rough surface to achieve the maximum shear resistance. Similar influence of surface roughness can be found on the initial stiffness. As summarized in Figure 13, under 20 kN axial pre-compression, the initial stiffness is 128.42 kN/mm for the interlocking brick prism with 0.1 mm surface roughness, which decreases to 83.55 kN/mm and 43.77 kN/mm when the surface roughness increases to 0.2 mm and 0.5 mm.

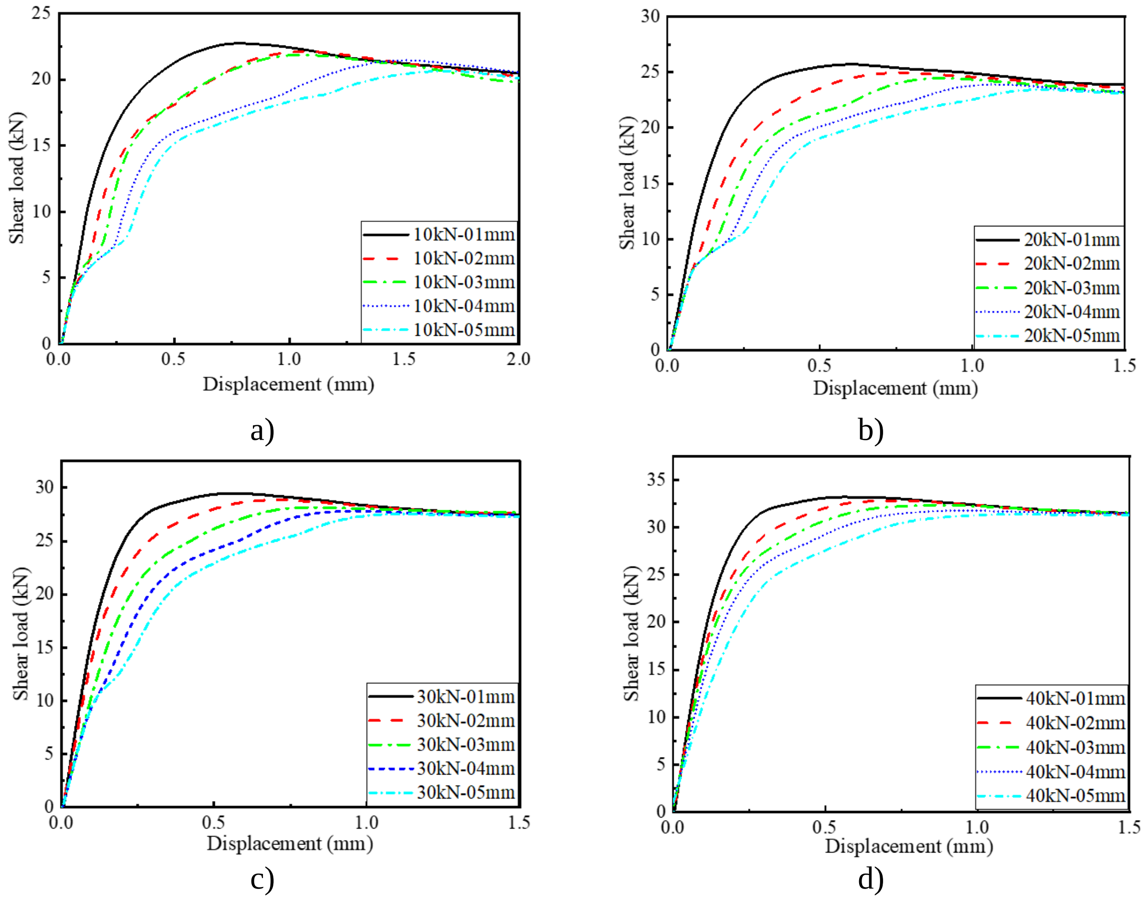


*Figure 12. Shear load versus displacement curves for interlocking brick with different surface roughness a) under 10kN axial pre-compression; b) 20 kN pre-compression; c) 30 kN pre-compression; d) 40 kN pre-compression*

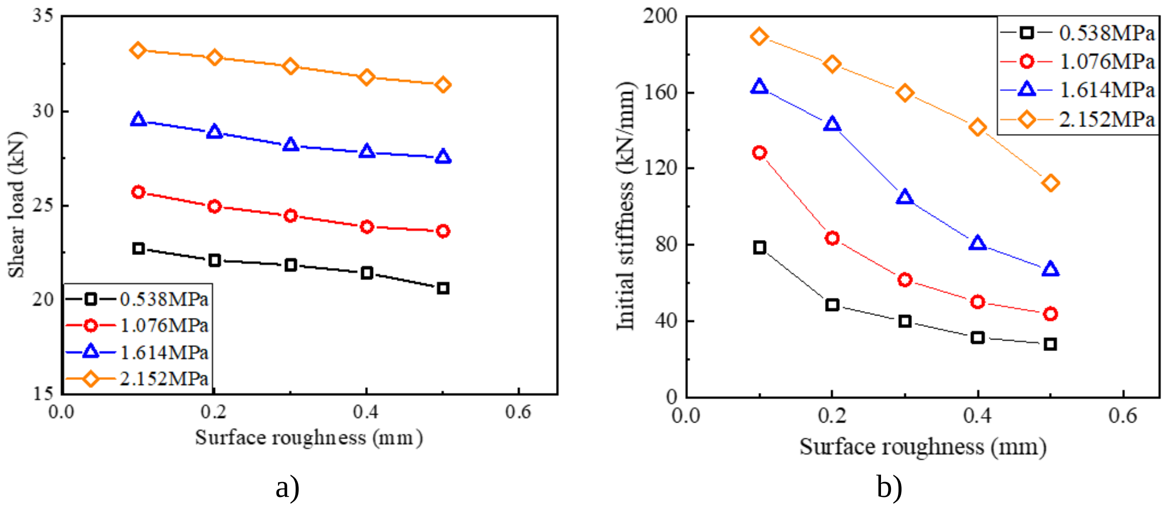


*Figure 13. Effect of the surface roughness on a) peak shear load; and b) initial stiffness*

## 6 Empirical Formula

The above results demonstrate existing analysis and design formulae may not provide accurate predictions of the shear resistance of the interlocking brick prism. This could be attributed to the different shear key failure mechanism, inappropriate surface friction coefficient used in the calculation, and lack of consideration of contact surface roughness [40]. Based on the laboratory test results and numerical parametric study results, a material failure based empirical prediction formula is proposed herein.

### 6.1 Material failure model

The following equation with reference to AASHTO is employed to define the shear resistance capacity of the interlocking brick prism as:

$$V_j = A_{key}^{V} f_c' (C_1 + C_2\sigma_n) + \mu A_{sm}\sigma_n \tag{5}$$

where $A_{key}^{V} f_c' (C_1+C_2\sigma_n)$ defines the contribution from the shear keys, and $\mu A_{sm}\sigma_n$ is the contribution from the friction resistance.

With large shear keys in interlocking bricks, the damage and failure of shear keys differ from those of small shear keys as defined in AASHTO. It is therefore necessary to properly re-examine the stress state and define the failure.

The failure envelope is employed herein which is based on the modification suggested by Hofbeck et al.[76]. The detailed derivation is presented in Appendix A. $C_1$ is the coefficient of shear strength, which takes into account the strength provided by interlocking keys ignoring the axial pre-compression, $C_1$, can be written as

$$C_1 = \frac{0.2125\cos\theta}{\sqrt{\left(\frac{1}{2}\times\frac{7A_{key}^{V}}{10A_{key}^{H}}\right)^2+1}-\frac{1}{2}\times\frac{7A_{key}^{V}}{10A_{key}^{H}}\sin\theta} \tag{6}$$

where $\theta$ is the inclined angle of the line $L_2$ relative to stress axis $\sigma$, which is tangent to the Mohr's circle at failure under uniaxial tension (see Figure A-2); $A_{key}^{H}$ is the horizontal projection area of the interlocking key along the direction of pre-compressive force, $A_{key}^{V}$ is the vertical projection area of the shear key along the direction of applied vertical force.

Considering brick material characteristic compressive strength $f_{cu,k}$ varying from 10 MPa to 30 MPa which are common range for concrete masonry units, and various interlocking brick geometry $A_{key}^{V}/A_{key}^{H}$, the coefficient factor $C_1$ can be calculated and shown in Figure 14. A conservative $C_1$=0.14 is determined with the current brick material strength and shear key geometry. As derived in the Appendix, when the axial pre-compression exists, the shear resistance by the shear key comprises coefficient $C_2$ which can be expressed as

$$C_2 = \frac{-B + \sqrt{B^2 - 4AC}}{2A\sigma_x f_c'} - \frac{0.2125\cos\theta}{\sigma_x\left(\sqrt{\left(\frac{1}{2} \times \frac{7A^V_{key}}{10A^H_{key}}\right)^2 + 1} - \frac{1}{2} \times \frac{7A^V_{key}}{10A^H_{key}}\sin\theta\right)} \tag{7}$$

where $\sigma_x$ is the normal stress due to axial pre-compression, and $f_c'$ is the concrete compressive strength; $A$, $B$ and $C$ represent the geometry coefficients (see Appendix A for the details).

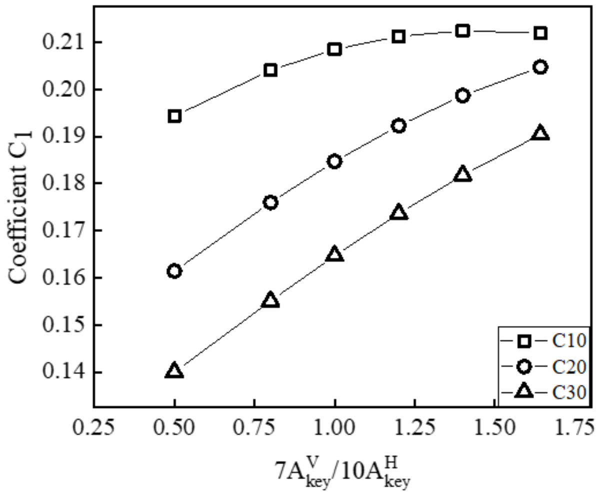


*Figure 14. Coefficient $C_1$ with respect to different geometries of interlocking key*

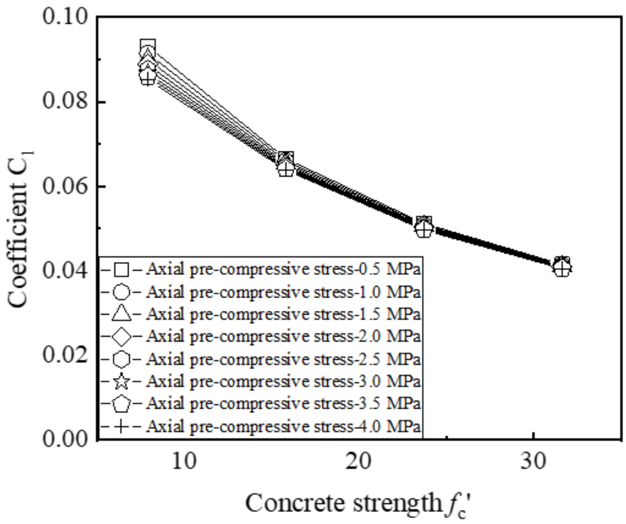


*Figure 15. Coefficient $C_2$ with varying material strength*

The variation of $C_2$ with material strength as well as axial pre-compression is shown in Figure 15. It is found that the coefficient $C_2$ changes insignificantly with axial pre-compression stress $\sigma_n$ ($\sigma_x = \sigma_n$ in Eq. 5). However, the coefficient $C_2$ decreases, as the material compressive strength increases. The relationship between the coefficient $C_2$ and material compressive strength $f_c'$ are linearly fitted and shown in Eq. (8).

$$C_2 = -0.002f_c' + 0.10076 \tag{8}$$

Substituting Eq. (8) and $C_1$= 0.14 into Eq. (5), the shear capacity of interlocking brick is expressed using the following equation.

$$V_j = A_{key}^V f_c'(0.14 + (-0.002f_c' + 0.10076)\sigma_n) + uA_{sm}\sigma_n \tag{9}$$

It is worth noting that this equation is applicable to the interlocking brick in this study, whose geometry was optimized with proved best mechanical performance [77].

## 6.2 Modified design formula

To consider the influence of the brick surface roughness, modification is made by introducing correction factors, $f(h_{imp})$ and $g(h_{imp})$ in the analytical solution of Eq. (9) based on the results from the numerical simulations and laboratory tests, which account for the influence of surface roughness on the shear resistance for the shear key and the rest flat regions. The shear capacity of an interlocking brick prism, $V_{j,imp}$, is given as follows:

$$V_{j,imp} = f(h_{imp}) \cdot A_{key}^V f_c'(0.14 + (-0.002f_c' + 0.10076)\sigma_n) + \mu \cdot g(h_{imp})A_{sm}\sigma_n \tag{10}$$

Regression analysis on the simulations and laboratory testing is carried out to obtain the above modification coefficients in the proposed formula. The coefficient of determination ($R^2$) is found to be 95.44% for Eq. (11), which shows the predicted results are in good agreement with the values from the test and numerical modelling. The predicted prism shear strength is positively related to the material compressive strength, and inversely proportional to the roughness amplitude.

$$V_{j,imp} = (-0.3033h_{imp} + 1.7519)A_{key}^V f'_c(0.14 + (-0.002f'_c + 0.10076)\sigma_n) + \mu(-0.0884h_{imp} + 0.5353)A_{sm}\sigma_n \tag{11}$$

where $h_{imp}$ is the surface roughness varying from 0.1 mm to 0.5 mm; $f_c'$ denotes material compressive strength varying from 10 MPa to 30 MPa; $\sigma_n$ stands for the normal stress from axial pre-compressive stress ranging from 0.54 MPa to 2.15 MPa; and $\mu$ is the friction coefficient ranging from 0.1 to 0.6.

The predicted shear strength using the above proposed formula, existing design methods, and laboratory testing data are compared in Figure 16. The AASHTO design specification and the theoretical prediction is unconservative in predicting the shear strength of the interlocking key. Rombach and Specker's formula underestimates the shear capacity when the pre-compression is low and overestimates it when the pre-compression is high. Using the modified design formula, the shear strength of the specimen with 10 kN pre-compression is estimated to be 1.048 MPa, which agrees well with the 1.17 MPa shear strength obtained from the laboratory tests, yielding only about 10% difference. When the pre-compression 30 kN, the shear strength is estimated to be 1.57 MPa, while the tested strength is 1.48 MPa, indicating a discrepancy of only 6%. Therefore, it can be concluded that the proposed formula can better predict the shear strength of the interlocking brick under different conditions as compared to the AASHTO, Rombach and Specher's method and existing theoretical prediction.

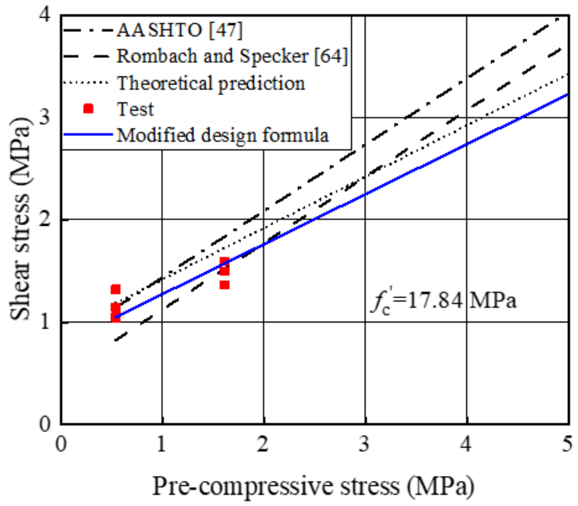


*Figure 16. Comparison between different design models*

## 7 Conclusions

In this study, numerical modeling and laboratory tests are conducted to investigate the shear behavior of interlocking brick. The failure modes of mortar-less interlocking brick prisms are investigated. Three-dimension (3D) numerical models of the interlocking brick prism are developed using three different contact modelling approaches, which are validated against the laboratory testing results. Parametric study is conducted to evaluate the influences of friction coefficient, axial pre-compression, brick material strength and interface roughness because of brick surface unevenness on the shear capacity. Combining the testing results and numerical simulation, a modified analytical formula is proposed for prediction of the shear strength capacity of the interlocking brick prism. The following conclusions have been drawn:

- Laboratory test and numerical modeling show the shear strength of the interlocking prism is dependent on the pre-compression level.

- Numerical simulations with three different contact modelling approaches demonstrate that modelling the brick surface roughness is important for the reliable prediction of interlocking brick shear behavior. The simplified rough contact model is found to be able to give a good prediction of prism initial stiffness, and shear capacities, whereas the model with perfect contact leads to large prediction error.
- Existing design and analysis method may not accurately predict the shear strength of the interlocking brick with large keys because of the different shear failure mechanism, negligence of interface roughness, and inappropriate friction coefficient.
- Parametric study evaluates the influences of the coefficient of friction, axial pre-compression, interface roughness, and material compressive strength on the interlocking prism shear strength.
- A modified analysis and design formula with consideration of brick surface condition is proposed for prediction of the shear capacity of interlocking brick prism.


## Acknowledgments

The authors would like to acknowledge the financial support from Australian Research Council under LP170100846 for carrying out this study.


## Reference


[1] Magenes G, Calvi GM. In-plane seismic response of brick masonry walls. Earthquake engineering & structural dynamics. 1997;26:1091-112.

[2] Ramamurthy K, Kunhanandan Nambiar E. Accelerated masonry construction review and future prospects. Progress in Structural Engineering and Materials. 2004;6:1-9.

[3] Wang GJ, Li YM, Zheng N, Ingham JM. Testing and modelling the in-plane seismic response of clay brick masonry walls with boundary columns made of precast concrete interlocking blocks. Engineering Structures. 2017;131:513-29.

[4] Rekik A, Allaoui S, Gasser A, Blond E, Andreev K, Sinnema S. Experiments and nonlinear homogenization sustaining mean-field theories for refractory mortarless masonry: The classical secant procedure and its improved variants. European Journal of Mechanics-A/Solids. 2015;49:67-81.

[5] Thanoon WA, Alwathaf AH, Noorzaei J, Jaafar MS, Abdulkadir MR. Nonlinear finite element analysis of grouted and ungrouted hollow interlocking mortarless block masonry system. Engineering Structures. 2008;30:1560-72.

[6] Shi TW, Zhang XH, Hao H, Chen C. Experimental and numerical investigation on the compressive properties of interlocking blocks. Engineering Structures.228:111561.

[7] Ngapeya GGC, Waldmann D, Scholzen F. Impact of the height imperfections of masonry blocks on the load bearing capacity of dry-stack masonry walls. 2018;165:898-913.
[8] Martínez M, Atamturktur S, Ross B, Thompson J. Assessing the compressive behavior of dry-stacked concrete masonry with experimentally informed numerical models. Journal of Structural Engineering. 2018;144:04018080.
[9] Sahu S, Sarkar P, Davis R. Quantification of uncertainty in compressive strength of fly ash brick masonry. Journal of Building Engineering. 2019;26:100843.
[10] Zhang X, Biswas WK. Development of eco-efficient bricks–A life cycle assessment approach. Journal of Building Engineering. 2021;42:102429.
[11] Ayed HB, Limam O, Aidi M, Jelidi A. Experimental and numerical study of interlocking stabilized earth blocks mechanical behavior. Journal of Building Engineering. 2016;7:207-16.
[12] Jaafar MS, Alwathaf AH, Thanoon WA, Noorzaei J, Abdulkadir M. Behaviour of interlocking mortarless block masonry. Proceedings of the Institution of Civil Engineers-Construction Materials. 2006;159:111-7.
[13] Sturm T, Ramos LF, Lourenço PB. Characterization of dry-stack interlocking compressed earth blocks. Materials and Structures. 2015;48:3059-74.
[14] Lee YH, Shek PN, Mohammad S. Structural performance of reinforced interlocking blocks column. Construction and Building Materials. 2017;142:469-81.
[15] Jaafar MS, Thanoon WA, Najm AMS, Abdulkadir MR, Ali AAA. Strength correlation between individual block, prism and basic wall panel for load bearing interlocking mortarless hollow block masonry. Construction and Building Materials. 2006;20:492-8.
[16] Anand KB, Ramamurthy K. Development and performance evaluation of interlocking-block masonry. Journal of Architectural Engineering. 2000;6:45-51.
[17] Sarfarazi V, Haeri H. Effect of number and configuration of bridges on shear properties of sliding surface. Journal of Mining Science. 2016;52:245-57.
[18] Shemirani AB, Haeri H, Sarfarazi V, Hedayat A. A review paper about experimental investigations on failure behaviour of non-persistent joint. Geomechanics and Engineering. 2017;13:535-70.
[19] Liu H, Liu P, Lin K, Zhao S. Cyclic behavior of mortarless brick joints with different interlocking shapes. Materials. 2016;9:166.
[20] Casapulla C, Mousavian E, Argiento L, Ceraldi C, Bagi K. Torsion-shear behaviour at the interfaces of rigid interlocking blocks in masonry assemblages: experimental investigation and analytical approaches. Materials and Structures. 2021;54:1-20.
[21] Anand K, Ramamurthy K. Development and performance evaluation of interlocking-block masonry. Journal of Architectural Engineering. 2000;6:45-51.
[22] Alwathaf AH, Thanoon WA, Jaafar MS, Noorzaei J, Kadir MRA. Shear characteristic of interlocking mortarless block masonry joints. Masonry International. 2005;18:39-44.
[23] Ali M, Gultom RJ, Chouw N. Capacity of innovative interlocking blocks under monotonic loading. Construction and Building Materials. 2012;37:812-21.
[24] Tang ZH, Ali M, Chouw N. Residual compressive and shear strengths of novel coconut-fibre-reinforced-concrete interlocking blocks. Construction and Building Materials. 2014;66:533-40.
[25] Li C, Hao H, Bi KM. Numerical study on the seismic performance of precast segmental concrete columns under cyclic loading. Engineering Structures. 2017;148:373-86.

[26] Li C, Hao H, Zhang XH, Bi KM. Experimental study of precast segmental columns with unbonded tendons under cyclic loading. Advances in Structural Engineering. 2017:319-34.
[27] Askar OF, Aziz AH, Al-Shaarbaf IA. Experimental study on the shear transfer in joints of precast segmental bridge. Journal of Engineering and Sustainable Development. 2012;16:88-106.
[28] Ahmed GH, Aziz OQ. Stresses, deformations and damages of various joints in precast concrete segmental box girder bridges subjected to direct shear loading. Engineering Structures. 2020;206:110151.
[29] Bu ZY, Wu WY. Inter shear transfer of unbonded prestressing precast segmental bridge column dry joints. Engineering Structures. 2018;154:52-65.
[30] Ahmed GH, Aziz OQ. Shear strength of joints in precast posttensioned segmental bridges during 1959–2019, review and analysis. Structures 2019;20:527-42.
[31] Alcalde M, Cifuentes H, Medina F. Influence of the number of keys on the shear strength of post-tensioned dry joints. Materiales de Construcción. 2013;63:297-307.
[32] Zhou XM, Mickleborough N, Li ZJ. Shear strength of joints in precast concrete segmental bridges. ACI Structural Journal. 2005;102:3.
[33] Jiang HB, Wei RB, Ma ZJ, Li YH, Jing Y. Shear strength of steel fiber-reinforced concrete dry joints in precast segmental bridges. Journal of Bridge Engineering. 2016;21:04016085.
[34] Jiang HB, Chen L, Ma ZJ, Feng WX. Shear behavior of dry joints with castellated keys in precast concrete segmental bridges. Journal of Bridge Engineering. 2015;20:04014062.
[35] Zhang XH, Hao H, Zheng JB, Hernandez F. The mechanical performance of concrete shear key for prefabricated structures. Advances in Structural Engineering. 2020;24:291-306.
[36] Buyukozturk O, Bakhoum MM, Beattie SM. Shear behavior of joints in precast concrete segmental bridges. Journal of Structural Engineering. 1990;116:3380-401.
[37] Jiang HB, Wang SD, Fang ZC, Chen GF, Li JH. Numerical analysis on the shear behavior of single-keyed dry joints in precast high-strength concrete segmental bridges. Mathematical Biosciences and Engineering. 2019;16:3144-68.
[38] Liu TX, Wang Z, Guo J, Wang JQ. Shear strength of dry joints in precast UHPC segmental bridges: experimental and theoretical research. Journal of Bridge Engineering. 2019;24:04018100.
[39] Gopal BA, Hejazi F, Hafezolghorani M, Lei VY. Numerical analysis and experimental testing of ultra-high performance fibre reinforced concrete keyed dry and epoxy joints in precast segmental bridge girders. International Journal of Advanced Structural Engineering. 2019;11:463-72.
[40] Shamass R, Zhou XM, Alfano G. Finite-element analysis of shear-off failure of keyed dry joints in precast concrete segmental bridges. Journal of Bridge Engineering. 2015;20:04014084.
[41] Ahmed GH, Aziz OQ. Influence of intensity & eccentricity of posttensioning force and concrete strength on shear behavior of epoxied joints in segmental box girder bridges. Construction and Building Materials. 2019;197:117-29.
[42] Agaajani S, Waldmann D. Stabilité de systèmes de murs en blocs de béton emboîtables sans joints en mortier. 2012.
[43] Agaajani S. Development and investigation of a new dry-stacked wall system [Ph.D]: University of Luxembourg; 2015.

[44] Fan WC, Cao P, Tang GD. Experimental and numerical study on the damage evolution of random rock joint surface during direct shear under CNL condition. Geotechnical and Geological Engineering. 2019;37:975-83.
[45] Thompson MK. Methods for generating rough surfaces in ANSYS. Proceedings of the 2006 International ANSYS Users Conference & Exhibition, Pittsburgh, PA2006.
[46] Thompson MK, Thompson J. Methods for generating probabilistic rough surfaces in ANSYS. Proc 20th Korea ANSYS User's Conf2010. p. 9-10.
[47] Thompson MK. A comparison of methods to evaluate the behavior of finite element models with rough surfaces. Scanning. 2011;33:353-69.
[48] Bahaaddini M, Sharrock G, Hebblewhite BK. Numerical direct shear tests to model the shear behaviour of rock joints. Computers and Geotechnics. 2013;51:101-15.
[49] Boutoutaou H, Bouaziz M, Fontaine JF. Modelling of interference fits with taking into account surfaces roughness with homogenization technique. International Journal of Mechanical Sciences. 2013;69:21-31.
[50] Hyun S, Pei L, Molinari JF, Robbins MO. Finite-element analysis of contact between elastic self-affine surfaces. Physical Review E. 2004;70:026117.
[51] Roberts CL, Breen JE, Kreger ME. Measurement based revisions for segmental bridge design and construction criteria. Austin (TX): The University of Texas at Austin: Center for Transportation Research, Bureau of Engineering Research; 1993.
[52] Turmo J, Ramos G, Aparicio AC. Shear strength of dry joints of concrete panels with and without steel fibres: Application to precast segmental bridges. Engineering Structures. 2006;28:23-33.
[53] Bakhoum MM. Shear behavior and design of joints in precast concrete segmental bridges [Ph.D]: Massachusetts Institute of Technology; 1990.
[54] Foure B, Bouafia Y, Soubret R, Thomas P. Shear test on keyed joints between precast segments. Proceedings of the Workshop AFPC External Prestressing in Structures, Saint-Rémy-lès-Chevreuse1993. p. 297-319.
[55] AASHTO. Guide specifications for design and construction of segmental concrete bridges. Section. 2nd ed; ed. 2003 interim revisions2003.
[56] Ahmed GH, Aziz OQ. Shear behavior of dry and epoxied joints in precast concrete segmental box girder bridges under direct shear loading. Engineering Structures. 2019;182:89-100.
[57] ASTM. Standard test methods for sampling and testing concrete masonry units and related units. ASTM C140-10. 2008.
[58] BS EN 1052-3: 2002: Methods of test for masonry- Part 3: determination of initial shear strength. British Standards Institution. 2002.
[59] Systèmes D. ABAQUS Documentation (Dassault Systèmes, Providence, RI). Version; 2014.
[60] Lubliner J, Oliver J, Oller S, Oñate E. A plastic-damage model for concrete. International Journal of Solids and Structures. 1989;25:299-326.
[61] Simulia. Abaqus Analysis User's Guide, Version 6.14. Dassault Systemes Providence, RI; 2014.
[62] Wang Z-q, Yu Z-w. Concrete damage model based on energy loss. Journal of Building Materials. 2004;7:365-9.
[63] Gorst NJS, Williamson SJ, Pallett PF, Clark LA. Friction in temporary works. Research Rep. 2003;71.
[64] Chahrour AH, Soudki KA, Straube J. RBS polymer encased concrete wall part I: experimental study and theoretical provisions for flexure and shear. Construction and Building Materials. 2005;19:550-63.

[65] Drygala I, Dulinska J, Jasienko J. Numerical evaluation of seismic-induced damages in masonry elements of historical arch viaduct. IOP Conference Series: Materials Science and Engineering: IOP Publishing; 2018. p. 012006.
[66] Kaneko Y, Connor JJ, Triantafillou TC, Leung CK. Fracture mechanics approach for failure of concrete shear key. I: Theory. Journal of Engineering Mechanics. 1993;119:681-700.
[67] Freund L. Stress intensity factor calculations based on a conservation integral. International Journal of Solids and Structures. 1978;14:241-50.
[68] Cholewicki A. Loadbearing capacity and deformability of vertical joints in structural walls of large panel buildings. Building Science. 1971;6:163-84.
[69] Koseki K, Breen JE. Exploratory study of shear strenght of joints for precast segmental bridges. University of Texas, Austin,1983.
[70] Bakhoum MM. Shear behavior and design of joints in precast concrete segmental bridges: Massachusetts Institute of Technology; 1990.
[71] Wong RH, Chau KT. Crack coalescence in a rock-like material containing two cracks. International Journal of Rock Mechanics and Mining Sciences. 1998;35:147-64.
[72] Rombach GA, Specker A. Segmentbrücken. Beton-Kalender, Teil 1,Ernst & Sohn. 2004:177-212.
[73] Specker A, Rombach GA. Design of joints in segmental hollow box girder bridges. 1st FIB Kongress. Osaka, Japan, 2002.
[74] Specker A. Der Einfluss der Fugen auf die Querkraft-und Torsionstragfähigkeit extern vorgespannter Segmentbrücken [Ph.D]: Technische Universität Hamburg; 2001.
[75] Sandoval C, Calderón S, Almazán JL. Experimental cyclic response assessment of partially grouted reinforced clay brick masonry walls. Bulletin of Earthquake Engineering. 2018;16:3127-52.
[76] Hofbeck JA, Ibrahim IO, Mattock AH. Shear transfer in reinforced concrete. Journal Proceedings1969. p. 119-28.
[77] Yong HTD. Utilisation of topologically-interlocking osteomorphic blocks for multi-purpose civil construction [Ph.D]: The University of Western Australia; 2011.
[78] AASHTO LRFD bridge design specifications. American Association of State Highway and Transportation Officials, Washington, DC. 2012.

## Appendix – Interlocking shear resistance model

The shear resistant mechanism of the interlocking brick prism comprises of two parts, i.e., shear keys and interface friction, which can be expressed as

$$V_j = A_{key}^{V} f_c' (C_1 + C_2 \sigma_n) + u A_{sm} \sigma_n \tag{A-1}$$

The contribution of shear key is influenced by material strength $f_c'$, normal stress from axial pre-compression $\sigma_n$, and shear key geometry. To determine coefficient $C_1$ and $C_2$, the influence of material shear strength on shear key resistance is analysed first. Figure A-1(a) illustrates the free body diagram of the interlocking brick prism. *V* is the applied vertical force on the brick prims. The force on each interlocking brick joint is *V*/2 due to symmetry. Since there are two shear keys on each joint bearing this force, the shear force $F_s$ on each shear key equals to *V*/4. Take a typical element on the shear key for stress analysis which experiences axial compressive stress $\sigma_x$ from axial pre-compression, shear stress $\tau$ and normal stress $\sigma_y$, which can be calculated with the applied forces on the prism as

$$\tau = \frac{F_S}{A_{key}^{V}} = \frac{V}{4A_{key}^{V}} \tag{A-2}$$

$$\sigma_x = \frac{N}{A_{brick}} \tag{A-3}$$

$$\sigma_y = \frac{7F_S}{10A_{key}^{H}} = \frac{7V}{40A_{key}^{H}} \tag{A-4}$$

where *V* is the applied vertical force on the brick prims, *N* is the axial pre-compression force, $A_{key}^{H}$ is the horizontal projection area of the interlocking key along the direction of pre-compressive force, and $A_{key}^{V}$ is the vertical projection area of the interlocking key along the direction of the applied vertical shear force, $A_{brick}$ is the cross-sectional area of the interlocking brick perpendicular to the axial pre-compression direction, as shown in Figure A-1(c). Detailed derivation of $\sigma_y$ is provided in Figure A-1.

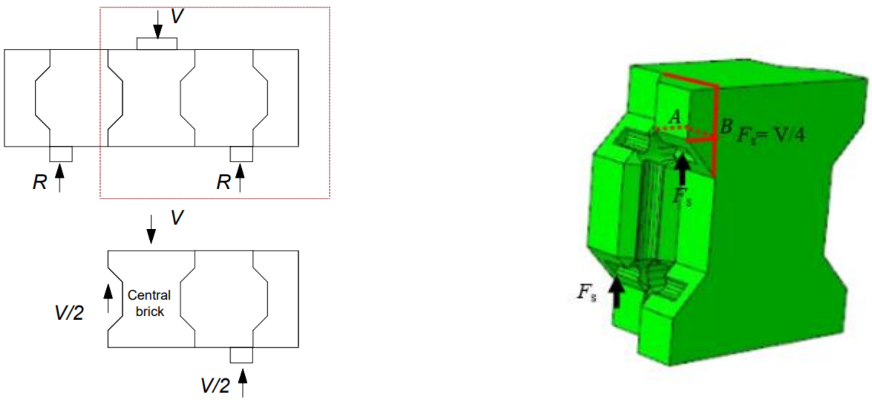

Central brick

(a) Free body diagram

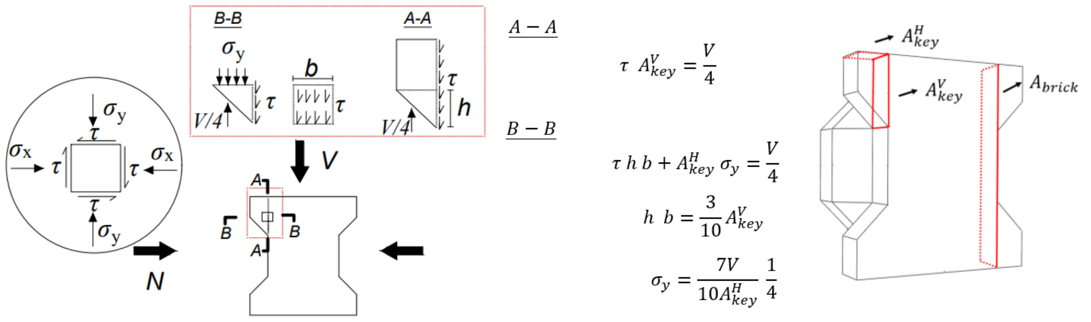


(b) Stress analysis (c) Geometry

*Figure A-1. Free body diagram and stress state*

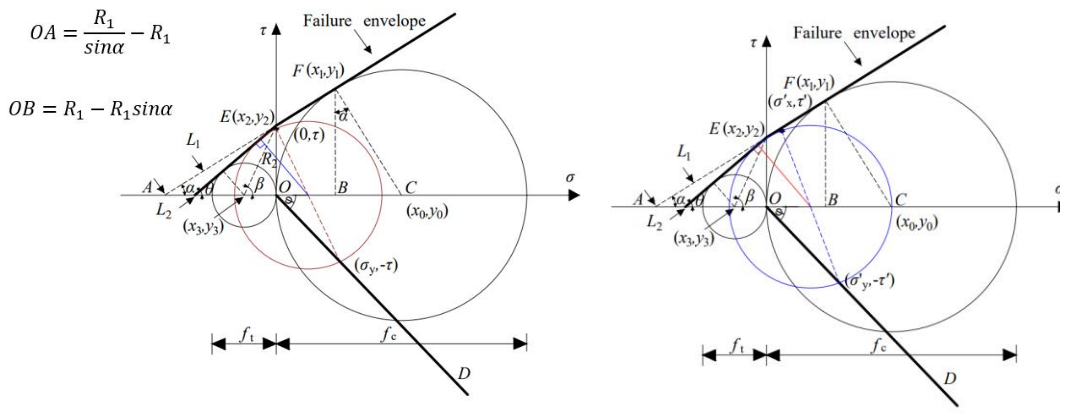


(a) No axial compressive stress $\sigma_x$ (b) With axial compressive stress $\sigma_x$

*Figure A-2. Stress state and failure envelope*

To define the failure of the brick, modified Mohr-Coulomb criteria is used. As shown in Figure A-2a, line $L_1$ defines the original concrete failure surface, which is inclined at α= 37° to the normal stress axis $\sigma$ and tangent to the Mohr's circle for uniaxial compression. The tangent point of $L_1$ with the Mohr's circle for uniaxial compression is $(x_1, y_1)$. The coordinate of $(x_1, y_1)$ can be written as

$$x_1 = x_0 - R_1 sin\alpha = f_c/2 - f_c/2 \cdot sin\alpha = f_c/2 \cdot (1 - sin\alpha) \quad \text{(A-5a)}$$

$$y_1 = y_0 + R_1 cos\alpha = 0 + f_c/2 \cdot cos\alpha = f_c/2 \cdot cos\alpha \quad \text{(A-5b)}$$

where α=37°, $R_1$ is radius of the Mohr's circle for uniaxial compression that equals to $f_c/2$.

The point of intersection of line $L_1$ with the $\tau$ axis is $(x_2, y_2)$, in which $x_2 = 0$. Considering triangle similarity rule between *AOE* and *ABF*, $y_2$ can be expressed as

$$y_2 = \frac{OA}{AB} \cdot y_1 = \frac{1}{1 + \frac{OB}{OA}} \cdot y_1 = \frac{1}{1 + \frac{R_1 - R_1 sin\alpha}{\frac{R_1}{sin\alpha} - R_1}} \cdot R_1 \cdot cos\alpha = f_c/2 \cdot \frac{cos\alpha}{1 + sin\alpha} \qquad \text{(A-6)}$$

Substituting α= 37° in Eq. A-6, $y_2$=0.25$f_c$.

Line $L_2$ is the modified concrete failure surface in the tensile region, which is drawn from the point of intersection with $\tau$ axis, and is tangent to the Mohr's circle for uniaxial tensive failure. The tangent angle is relative to stress axis is $\theta$. The centre coordinate of the uniaxial tensile strength circle is ($x_3$, $y_3$) =(-$f_t$/2, 0). The angle of the line connecting point ($x_2$, $y_2$) and ($x_3$, $y_3$) relative to $\sigma$ axis is β, which can be calculated by

$$tan\beta = \left|\frac{y_2}{x_3}\right| = \frac{0.25f_c}{f_t/2} = 0.5\frac{f_c}{f_t} \qquad \text{(A-7a)}$$

$$\beta = tan^{-1}(0.5\frac{f_c}{f_t}) \qquad \text{(A-7b)}$$

Typically for concrete like material, the uniaxial compression strength $f_c$ is taken as 0.85 $f_c'$ and the tensile strength $f_t$ is taken as $0.604\sqrt{f_c'}$ MPa [78]. Therefore,

$$\beta = tan^{-1}(0.7\sqrt{f_c'}) \qquad \text{(A-8)}$$

The angle for the modified failure envelop can be calculated by

$$\theta = 2\beta - 90^\circ \qquad \text{(A-9)}$$

To determine $C_1$ in Eq. A-1, take a stress state of non-confinement $\sigma_x$=0, when the stress reaches the failure state under gradually increased shear load, line $L_2$ is tangent to the Mohr's circle, and runs across line OD at point ($\sigma_y$,$-\tau$). The point of intersection of the Mohr's circle with the $\tau$ axis is (0, $\tau$). The distance from centre of the Mohr's circle, i.e., point ($\sigma_y$/2, 0), to Line $L_2$ is

$$R_2 = \left(\frac{y_2}{tan\theta} + \frac{\sigma_y}{2}\right) sin\theta \qquad \text{(A-10a)}$$

where $R_2$ is radius of the Mohr's circle.

Substituting Eqs. A-2, A-4 and A-6 into A-10 together with α=37°, it yields

$$R_2 = 0.25 \cdot f_c \cdot cos\theta + \left(\frac{7A_{key}^V}{10A_{key}^H}\right) \cdot \frac{\tau}{2} \cdot sin\theta \qquad \text{(A-10b)}$$

Since the radius of the stress circle $R_2$ can also be written as

$$R_2 = \sqrt{(\sigma_y - \frac{\sigma_y}{2})^2 + (-\tau - 0\,)^2} \qquad \text{(A-11a)}$$

Substituting Eq. A-2 and A-4 in,

$$R_2 = (\sqrt{(\frac{1}{2} \times \frac{7A_{key}^V}{10A_{key}^H})^2 + 1})\tau \qquad \text{(A-11b)}$$

With Eqs. A-10b and A-11b, the shear stress τ is expressed using the following equation.

$$\tau = \frac{0.25 \cdot f_c \cdot cos\theta}{\sqrt{(\frac{1}{2} \times \frac{7A_{key}^{V}}{10A_{key}^{H}})^2 + 1} - \frac{1}{2} \times \frac{7A_{key}^{V}}{10A_{key}^{H}} sin\theta} = \frac{0.2125 f_c{}' cos\theta}{\sqrt{(\frac{1}{2} \times \frac{7A_{key}^{V}}{10A_{key}^{H}})^2 + 1} - \frac{1}{2} \times \frac{7A_{key}^{V}}{10A_{key}^{H}} sin\theta} \tag{A-12}$$

Using Eq. A-12, the coefficient $C_1$ in Eq. A-1 can be expressed with variables $A_{key}^{V}$, $A_{key}^{H}$ related to shear key geometry and concrete failure angle $\theta$.

$$C_1 = \frac{0.2125 cos\theta}{\sqrt{(\frac{1}{2} \times \frac{7A_{key}^{V}}{10A_{key}^{H}})^2 + 1} - \frac{1}{2} \times \frac{7A_{key}^{V}}{10A_{key}^{H}} sin\theta} \tag{A-13}$$

To determine the coefficient $C_2$, when the interlocking brick is subjected to axial pre-compressive stress, $\sigma_x$ is introduced and the corresponding Mohr's circle enlarges, which is nevertheless still tangent to the strength envelope line $L_2$. As shown in Figure A-2b, point ($\sigma'_x$, $\tau'$) and ($\sigma'_y$, $-\tau'$), respectively. The centre coordinates of the Mohr's circle is ($\frac{\sigma'_x+\sigma'_y}{2}$, 0). The radius of the circle can be calculated as

$$R_3 = \sqrt{\tau'^2 + (\frac{\sigma'_x}{2} - \frac{\sigma'_y}{2})^2} \tag{A-14}$$

Similar to Eq. A-10, line $L_2$ is tangent to the Mohr's circle. So the radius can also be calculated as

$$R_3 = \left(\frac{y_2}{tan\theta} + \frac{\sigma'_x + \sigma'_y}{2}\right) sin\theta = 0.25 \cdot f_c \cdot cos\theta + \left(\frac{\sigma'_x}{2} + \frac{\sigma'_y}{2}\right) sin\theta \tag{A-15}$$

With Eq. A-14 and A-15, the quadratic equation of shear stress τ is expressed using the following equation.

$$A\tau^2 + B\tau + C = 0 \tag{A-16}$$

where the coefficient A, B and C can be written as

$$A = 1 + \left(\frac{1}{2} \times \frac{7A_{key}^{V}}{10A_{key}^{H}}\right)^2 \cdot cos^2\theta \tag{A-17a}$$

$$B = -[\sigma_x(1 + sin^2\theta) + (0.5 f_c \cdot sin\theta cos\theta)] \cdot (\frac{1}{2} \times \frac{7A_{key}^{V}}{10A_{key}^{H}}) \tag{A-17b}$$

$$C = \left(\frac{\sigma_x^2}{4}\right) cos^2\theta - 0.25\sigma_x \cdot f_c \cdot sin\theta cos\theta - 0.0625 f_c^2 \cdot cos^2\theta \tag{A-17c}$$

The root of Eq. A-16 is expressed as follows:

$$\tau = \frac{-B + \sqrt{\mathrm{B}^2 - 4AC}}{2A} \qquad \text{(A-18)}$$

The shear stress under pre-compression can be written as

$$\tau = \frac{-B + \sqrt{\mathrm{B}^2 - 4AC}}{2A} - \frac{0.2125 f_c{}' cos\theta}{\sqrt{(\frac{1}{2} \times \frac{7A_{key}^V}{10A_{key}^H})^2 + 1} - \frac{1}{2} \times \frac{7A_{key}^V}{10A_{key}^H} sin\theta} \qquad \text{(A-19)}$$

Referring to Eq. (A-1), the coefficient $C_2$ is expressed using the following equation.

$$C_2 = \frac{-B + \sqrt{\mathrm{B}^2 - 4AC}}{2A\sigma_x f_c{}'} - \frac{0.2125 cos\theta}{\sigma_x(\sqrt{(\frac{1}{2} \times \frac{7A_{key}^V}{10A_{key}^H})^2 + 1} - \frac{1}{2} \times \frac{7A_{key}^V}{10A_{key}^H} sin\theta)} \qquad \text{(A-20)}$$